Biomedical Physics & Engineering Express

ENDORSED BY IPEM Institute of Physics and Engineering in Medicine

PAPER

Imaging of cell membrane topography using Tamm plasmon coupled emission

To cite this article: Shiekh Zia Uddin and Muhammad Anisuzzaman Talukder 2017 *Biomed. Phys. Eng. Express* **3** 065005

Biomedical Physics & Engineering Express

PAPER

Imaging of cell membrane topography using Tamm plasmon coupled emission

RECEIVED
4 May 2017

REVISED
7 August 2017

ACCEPTED FOR PUBLICATION
24 August 2017

PUBLISHED
17 November 2017

Shiekh Zia Uddin[1] **and Muhammad Anisuzzaman Talukder**[1,2]

[1] Department of Electrical and Electronic Engineering, Bangladesh University of Engineering and Technology, Dhaka 1205, Bangladesh
[2] School of Electronic and Electrical Engineering, University of Leeds, Leeds LS2 9JT, United Kingdom

E-mail: anis@eee.buet.ac.bd

Keywords: Tamm plasmon coupled emission, cell membrane topography, total internal reflection fluorescence microscopy

Abstract

Imaging of cell membrane topography is important for a clear understanding of the various biological activities of cells. We propose a technique for imaging the cell membrane topography that uses a metal-photonic crystal structure instead of a glass-water interface used in conventional polarized total internal reflection fluorescence microscopy (pTIRFM) techniques. Through the metal-photonic crystal of the proposed technique, the fluorophore labels on the cell membrane can be excited by both the *p*- and *s*-polarized excitation light, and in each case, the *p*- and *s*-polarized radiation from the excited fluorophores can be separated to form an image. We calculate the images of the cell membrane topography that is fusing a granule using the proposed technique and pTIRFM. The image obtained by the proposed technique shows a much greater contrast with respect to the background than that of the image obtained by pTIRFM. We also find that the structural similarity index of the image obtained by the proposed technique to a reference image is ~77%, which is only ~16% for the image obtained by pTIRFM. The proposed technique will help to obtain a clearer and more accurate image of the cell membrane topography, and hence, a deeper understanding of different biological activities.

1. Introduction

The cell membrane defines the physical boundary of a cell as a semi-permeable barrier between the intracellular components and the extracellular environment. The cell membrane controls the movement of substances into and out of the cells. The cell membrane also provides shape to the cells and helps the cells to migrate and undergo shape changes [1–3]. The local topography of the cell membrane changes due to a number of biological phenomena such as when the cells actively transport molecules into or out of the cells, i.e., during endocytosis and exocytosis, and when the cell membrane fuses with a vesicle [4–10]. Study of these important biological phenomena is crucial to understand how a cell interacts with the surrounding environment, which requires imaging the temporal and spatial topographical changes of the cell membrane.

Various electronic techniques such as atomic force microscopy, scanning ion conductance microscopy, and electron microscopy, as well as various optical techniques such as interference reflection microscopy, total internal reflection fluorescence microscopy, photoactivated localization microscopy, and confocal microscopy have been developed to image the cell membrane [11–16]. While the electronic microscopy techniques provide a much higher resolution than that of the optical microscopy techniques, the high energy electrons used in the electronic microscopy techniques usually destroy live cells [17]. Therefore, the electronic microscopy techniques cannot be applied to study the real-time changes in the cell membrane. Additionally, the electronic microscopy techniques require an extensive sample preparation, which makes them less suitable for studying biological phenomena. By contrast, while optical microscopy techniques do not destruct the live cells and require less sample preparation, the change in the index of refraction due to the change in the topography of membrane is small so that imaging with phase-based methods often fails to capture features of the membrane topography [18]. In confocal microscopy, images are formed from the collection of fluorescence that is emitted from a sample-depth of nearly a wavelength. Therefore, if confocal microscopy technique is used to image the cell

membrane, the background noise becomes too strong as the thickness of the cell membrane is much smaller than the wavelength of the incident light. However, the excitation depth of the sample can be limited to a thin region of ~100 nm, and therefore, a high signal-to-noise ratio can be achieved using total internal reflection fluorescence microscopy (TIRFM). Therefore, TIRFM is suitable for imaging small structures or molecular assemblies as well as the cell membrane topography [4].

A modified version of TIRFM, i.e., polarized total internal reflection fluorescence microscopy (pTIRFM), is particularly suitable for imaging the cell membrane topography, as it uses the interplay of the polarization of the excitation light and the orientation of the cell membrane to image the topography [19–21]. In pTIRFM, the cell membrane is labeled with a lipid fluorophore probe, e.g., diI, that has its dipole moment lying parallel to the membrane surface. The labeled membrane sample is excited sequentially by evanescent *p*- and *s*-polarized light, so that the fluorophores with horizontal and vertical dipole moments are excited separately. The *p*- and *s*-images acquired by the *p*- and *s*-polarized excitations provide information about the orientation of dipole moments of the fluorophores that are embedded within the cell membrane. Therefore, in essence, *p*- and *s*-images, and their ratio *p*/*s*-image provide information about the local orientation of the membrane [22, 23].

If a thin metal film is placed between the fluorophores and glass substrate of a pTIRFM structure, the power coupled to the glass substrate and the far-field radiation pattern for horizontally and vertically oriented fluorophores change significantly from that in a structure without the metal layer [24–28]. Due to the presence of the metal layer, a highly polarized and sharply directed angular light cone known as surface plasmon coupled emission (SPCE) is created from the metal-glass substrate interface [29–31]. SPCE has important applications in microscopy and sensing of bio-molecules [32–34]. An SPCE-based technique has a very low detection volume compared to other surface-based techniques as both the excitation field of the fluorophores and the coupled field to the metal layer from the excited fluorophores decay sharply with the distance of the fluorophores from the metal layer [35–39]. However, in an SPCE-based technique, fluorophores cannot be excited by *s*-polarized light, as the transmittance of *s*-polarized light is very low for a thin metal film [29, 40]. Therefore, if used for imaging the cell membrane, an SPCE-based technique cannot provide similar amount of information about the fluorophore orientation as provided by pTIRFM technique. Recently, a hybrid photonic-plasmonic structure has been proposed to modify the radiation of fluorophores, where a one-dimensional photonic crystal structure is attached between a metal layer and a glass substrate with the fluorophores placed on the metal layer [41–45]. Such a structure supports surface plasmons in metal-superstrate interface and Tamm plasmons in metal-photonic crystal interface [46]. The radiation of fluorophores couples to Tamm plasmons and causes directional radiation in the substrate, which is called Tamm plasmon coupled emission (TPCE). In contrast to what happens in an SPCE structure, in a TPCE structure, fluorophores can be excited by both *p*- and *s*-polarized light when excitation light is incident through the glass substrate. Also, a TPCE structure can be designed in a way so that fluorophores with horizontal and vertical dipole moments radiate at different angles through the substrate.

In this work, we propose a novel approach of imaging the cell membrane topography based on TPCE. In our proposal, a fluorescently labeled cell membrane should be placed on a TPCE structure that has different reflectance minima angles for incident *p*- and *s*-polarized light at both excitation and emission wavelengths. The fluorophores are excited separately by *p*- and *s*-polarized light. The emission of the excited fluorophores depends on the orientation of the fluorophores. The orientation-dependent emission can be collected through the TPCE structure as it has two reflection minima angles for *p*- and *s*-polarized light. If fluorophores are oriented along the orientation of the cell membrane, the collected light at two different reflectance minima angles for each of *p*- and *s*-polarized excitations can be used to make an image of the orientation or topography of the cell membrane. In this work, we develop a step-by-step theoretical approach to calculate the created image of the cell membrane using the proposed technique. We apply the developed theoretical approach to calculate the image of a diI-labeled cell membrane that is fusing a granule. We find that the image obtained using the proposed technique has a much greater contrast ratio with respect to the background noise when compared to that obtained using a pTIRFM technique. For a quantitative analysis of the quality of the obtained images, we calculate the structural similarity (SSIM) indices of the images obtained using the proposed and pTIRFM techniques with respect to a reference image. We find a maximum SSIM of ~77% for the image obtained using the proposed technique, which is ~16% for the image obtained using a pTIRFM technique.

The rest of the paper is organized as follows: in section 2, we present and discuss the proposed technique and the TPCE structure used in the proposed technique. In section 3, we present and discuss a feasible experimental setup for the proposed technique. In section 4, we develop a step-by-step theoretical approach to calculate the image obtained using the proposed technique. In section 5, we describe the steps to be carried out to obtain images of the cell membrane topography using the proposed technique. In section 6, we apply the proposed technique to theoretically create an image of the cell membrane that is fusing a granule. We compare the proposed technique

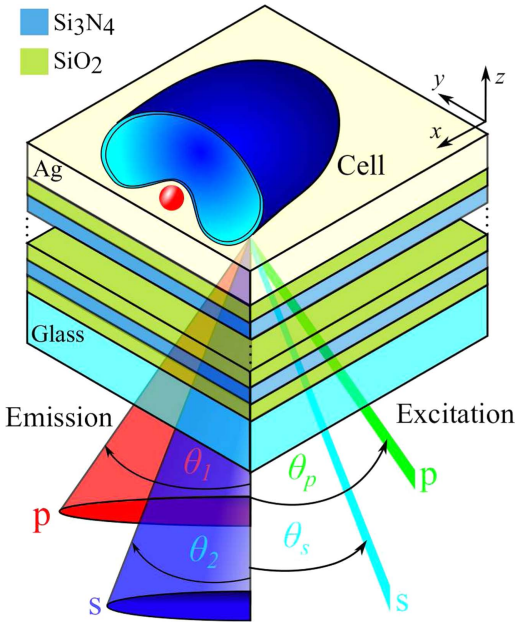

Figure 1. Schematic illustration of the proposed technique. A one-dimensional photonic crystal is placed over a glass substrate and a thin silver layer is deposited on the photonic crystal. The cell is placed over the metal layer. Fluorophores on the cell membrane can be excited by *p*- and *s*-polarized light incident at different angles. The emission from the fluorophores coming out in the glass side are sharply directed at two different angles.

with pTIRFM by calculating SSIM indices of the images obtained by both techniques with respect to a reference image. In section 7, we draw conclusions on the findings.

2. Proposed technique

We show a schematic illustration of the proposed technique in figure 1. In the proposed technique, the fluorescently labeled cell membrane is placed on a metal layer, which is deposited on a one-dimensional photonic crystal. A glass substrate holds the metal-photonic crystal structure. When light is incident on the metal layer from the radiating fluorophores, Tamm plasmon modes are excited at the metal-photonic crystal interface and light is emitted at multiple sharply directed angles through the glass substrate [41, 47]. In this work, we design a TPCE structure that has different reflectance minima angles for *p*- and *s*-polarized light at both excitation and emission wavelengths of the fluorophore. We denote the reflectance minima angles as θ_p and θ_s for *p*- and *s*-polarized incident light, respectively, at the excitation wavelength of the fluorophore. The different reflectance minima angles for *p*- and *s*-polarized light allow the fluorophores to be excited by either *p*-polarized excitation light incident at *p*-polarized reflectance minimum angle or *s*-polarized excitation light incident at *s*-polarized reflectance minimum angle through the glass substrate as shown in figure 1.

Table 1. Refractive indices of the layers in the designed structure.

Layer	Refractive index at 549 nm	Refractive index at 565 nm
Intracellular components [77]	1.38	1.38
Environment [77]	1.38	1.38
Metal (Ag) [78]	$0.043776 + j3.6013$	$0.045240 + j3.7405$
SiO_2 [79]	1.4600	1.4593
Si_3N_4 [80]	2.0234	2.0205
Glass prism	1.5186	1.5178

The fluorophores emit at two different angles through the structure when they are excited by either *p*- or *s*-polarized light. We denote the reflectance minima angles as θ_1 and θ_2 for *p*- and *s*-polarized incident light, respectively, at the emission wavelength of the fluorophore. In the proposed technique, the sample is first excited by *p*-polarized light, which results in two images collected at θ_1 and θ_2. Then the sample is excited by *s*-polarized light, which results in two more images collected at θ_1 and θ_2. These four images and their ratios provide information about the orientation of the cell membrane.

The designed one-dimensional photonic crystal for the proposed technique consists of alternating layers of relatively low index (L) SiO_2 and relatively high index (H) Si_3N_4 materials. SiO_2 and Si_3N_4 layers have thicknesses of 65 nm and 100 nm, respectively. The sequence of SiO_2 and Si_3N_4 layers, starting from the layer immediately on the glass substrate, can be written as $(HL)_5H$. The metal layer is a 50-nm-thick silver layer. The cell, immersed in water, is placed on the metal layer. The aqueous extracellular environment, the cell membrane, and the intracellular components create a three-layer system in the sample [48]. Since the sample penetration depth of the excitation field is on the order of ~150 nm, which is much smaller than the thickness of a cell, which is typically on the order of ~1 μm, the intracellular components can be assumed to extend to infinity in the *z*-direction [49]. The thin cell membrane of only ~10 nm can be neglected in calculations as it does not affect the results [50]. We assume the sample to have the refractive index of cytosol as also has been assumed in [19, 23, 51]. Therefore, the cell sample is modeled as a uniform medium with a refractive index of the cytosol and the cell membrane is modeled as a surface of infinitesimal thickness. However, in practice, there may be some scattering of the excitation light as well as of the light emitted by the dil fluorophores due to the non-uniform refractive indices in the intracellular components, cell membrane, and extracellular environment. The scattering due to non-uniform refractive indices may decrease the collection efficiency and lead to collection of the scattered field as noise. The refractive indices of different materials are given in table 1.

We calculate the reflectance characteristics of the designed TPCE structure with the cell placed on the

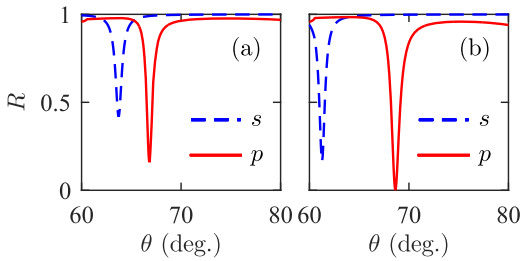

Figure 2. Angle-resolved reflectance characteristics (R) of the proposed structure for light incident at (a) 549 and (b) 565 nm.

metal layer against incidence angles by Berreman's 4×4 matrix method [52–54]. In figure 2(a), we show the reflectance profile of the structure for light incident from substrate side at the excitation wavelength of the dil fluorophore. The reflectance profile at the excitation wavelength has two different minima for p- and s-polarized incident light, i.e., $\theta_p = 66.8°$ and $\theta_s = 63.7°$. In figure 2(b), we show the reflectance profile of the structure for light incident from metal side at the emission wavelength of the dil fluorophore. The reflectance profile at the emission wavelength has two different minima for p- and s-polarized incident light, i.e., $\theta_1 = 68.8°$ and $\theta_2 = 61.3°$. In the proposed technique, the emission through the glass substrate can be collected by a high numerical aperture objective and selectively sent to an image acquiring mechanism through a confocal aperture similar to that used in [37, 55].

Although we have used SiO_2 and Si_3N_4 layers to design the proposed TPCE structure, other material systems such as GaAs/AlGaAs, GaAs/AlAs, and SiO_2/TiO_2 can be used as well [56–59]. In the proposed technique, the obtained images will mainly depend on the reflectance characteristics of the Tamm plasmon structure, which depend on the thicknesses of the alternating layers. Similar reflection characteristics, as shown in figure 2, can be achieved with appropriate layer thicknesses of GaAs/AlGaAs, GaAs/AlAs, and SiO_2/TiO_2 material systems. The alternating dielectric layers and silver metal layer of the proposed structure can be grown using plasma enhanced chemical vapor deposition (PECVD) and sputtering techniques, respectively. Although PECVD and sputtering techniques are widely used to grow sharp interfaces between alternating dielectrics and metal layers, the layer thicknesses may have an uncertainty or roughness on the order of ~1 nm in practice [60–62]. Therefore, the designed layer thicknesses of dielectric materials and metal in the proposed structure may vary by $\lesssim$2% in an actual structure, which is not significant to alter the behavior of the designed structure. To find out the change in the reflectance characteristics due to uncertainty in the growth of the dielectric materials and metal, we simulated cases with SiO_2 thickness 65 ± 4 nm, Si_3N_4 thickness 100 ± 5 nm, and silver layer thickness 50 ± 5 nm. In each case, we found that the angles corresponding to two reflection minima are separated by at least twice of the full-width at half-maximum (FWHM) of the reflectance curves. Therefore, even if the layer thicknesses vary significantly from the design values, the reflectance profiles for p- and s-polarized light will not overlap and the performance of the proposed technique will not change noticeably. We also note that the Tamm plasmon structures have shown reproducible characteristics and theoretical predictions calculated with designed values of the layer thicknesses have matched well with the experimental findings [41, 42].

While the reflectance minima angles may change noticeably when the layer thicknesses change, the FWHM of the reflectance spectra does not change much. In the proposed technique, the FWHM of the reflectance spectra should be less than the separation between the p- and s-polarized minima angles. The FWHM of the reflectance spectra mainly depends on the damping rate of the metal [40]. The higher the damping rate in the metal, the lower the Q-factor and the greater the FWHM of the reflectance spectra become. In the designed structure, the separation between the reflection minima for p- and s-polarized incidence is 3.1°. Silver is a low-loss metal that is widely used for plasmonic structures, and a FWHM of $\lesssim 1°$ is achievable in the proposed structure.

3. Feasible experimental setup

Now, we discuss the feasibility of practical implementation of the proposed technique. The overall experimental setup for the proposed technique will not be much different from that for pTIRFM technique, which has been used for studying the cell membrane dynamics for about two decades [19, 23]. TIRFM-based systems have been developed to precision and are commercially available [63]. TIRFM and pTIRFM systems are usually built on an inverted microscope, where both the light that excites the sample and the light that is collected from the emission of fluorophores pass through the objective lens [64]. The differences in the implementation of the proposed technique from pTIRFM lie in using a glass coverslip coated with metal-photonic crystal Tamm plasmon structure instead of a simple glass coverslip, exciting the sample at two different angles for p- and s-polarized light, and collecting and separating fluorescence emitted through two different angles. A detail discussion on fabrication and preparation of the coverslip that can be used in the proposed technique can be found in [42]. In figure 3, we show a schematic illustration of a feasible experimental setup for the proposed technique. In the following, we discuss the excitation and collection mechanisms in detail.

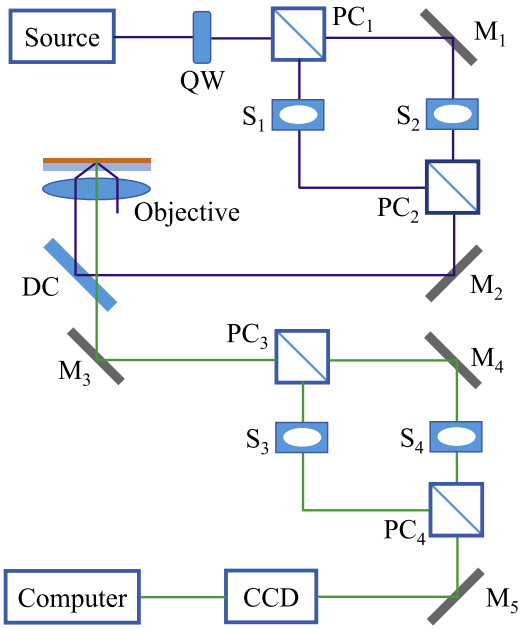

Figure 3. Schematic illustration of a feasible experimental setup for the proposed technique.

3.1. Excitation of fluorophores

As shown in figure 3, the linearly polarized light from a laser source will pass through a quarter-wave plate so that the polarization of light changes to circular or elliptical. The circularly or elliptically polarized light will be incident on a polarization cube PC_1, which reflects the vertical component but passes the horizontal component of the electric field. The vertical and horizontal components will become *p*- and *s*-polarized excitation light, respectively. A second polarization cube PC_2 and mirror M_1 will recombine the vertical and horizontal components of the electric field. Since *p*- and *s*-polarized light will illuminate the sample sequentially, two shutters S_1 and S_2 will be used to control the vertical and horizontal components. The light coming out of PC_2 will be reflected by mirror M_2 on to the dichroic mirror DC. DC will act as a longpass filter and will spectrally separate the excitation and emission light by reflecting and transmitting as a function of wavelength. The reflected light by DC will pass through the objective lens and incident on the coverslip at reflection minimum angle to excite the sample. The objective lens will change position so that *p*- and *s*-polarized light can be incident at θ_p and θ_s angles, respectively. Therefore, the control of the objective lens will be coupled to the control of shutters S_1 and S_2.

3.2. Collection of fluorescence

The light emitted by the fluorophores will be available at θ_1 and θ_2 angles, and will be focused to a point by the objective lens. For the designed TPCE structure $\theta_1 > \theta_2, \theta_p, \theta_s$. Therefore, maximum numerical aperture required for the proposed system is ~1.37, which is smaller than ~1.47 that is usually obtained in available objective lens [65, 66]. The emission light coming out of the objective lens will pass through DC and will be reflected by mirror M_3. The reflected light will be incident on polarization cube PC_3 and will be separated into vertical and horizontal components that are transmitted through θ_1 and θ_2 angles. The vertical and horizontal components will be added by another polarization cube PC_4 and mirror M_4. Shutters S_3 and S_4 will control the collection of vertical and horizontal components of the electric field. The control of shutters S_3 and S_4 will be coupled to the control of shutters S_1 and S_2. For each of S_1 and S_2 turn-on periods, S_3 and S_4 will turn on and off sequentially so that for each polarization of incident light, two images can be captured for emission at θ_1 and θ_2 angles. The light coming out of PC_4 will be reflected by mirror M_5 and captured on an electron-multiplying charge-coupled device (CCD) camera, which will be connected to a computer for post-processing of the captured images.

We note that the shutters and objective lens will be controlled by microprocessors and their operational parameters will be set in the imaging software [64]. The position of the objective lens can be precisely controlled to focus light on the coverslip at either θ_p or θ_s without any noticeable error. The objective lens can be controlled piezoelectrically over a broad range of $\gtrsim$1 mm with a fine resolution of ~1 nm [67]. The time required to excite the sample and capture one set of images using the proposed technique will be limited by the shutter speed and the speed at which the objective lens can change position for *p*- and *s*-polarized incident light. The speed of the state-of-the-art shutters is on the order of ~25 ms [63, 68]. While a motorized control of the objective lens can be cheaper, piezoelectrically controlled objective lens can step and settle in only ~20 ms [67]. Therefore, we can expect that a set of images will be captured in few hundred milliseconds using the proposed technique. Since biological phenomena related to the cell membrane usually occur on a time scale from tens of minutes to several hours, the proposed technique will be well suitable for capturing real-time changes of the cell membrane.

4. Theoretical modeling

4.1. Collected fluorescence from a distribution of fluorophores

Fluorophores are molecules that absorb light at a certain frequency and emit light at a different frequency. If an external electric field $\mathbf{E}^{\mathbf{ex}}$ is incident on a fluorophore that has a unit dipole moment $\boldsymbol{\mu}^{\mathbf{ex}}$, the power absorbed by the fluorophore is proportional to $|\boldsymbol{\mu}^{\mathbf{ex}} \cdot \mathbf{E}^{\mathbf{ex}}|^2$, which is called the excitation probability [69, 70]. The emission characteristics of the excited fluorophore can be calculated by modeling it as an electric dipole that has a moment $\boldsymbol{\mu}^{\mathbf{em}}$, where $|\boldsymbol{\mu}^{\mathbf{em}}| = 1$. If the fluorophore is situated near a planar

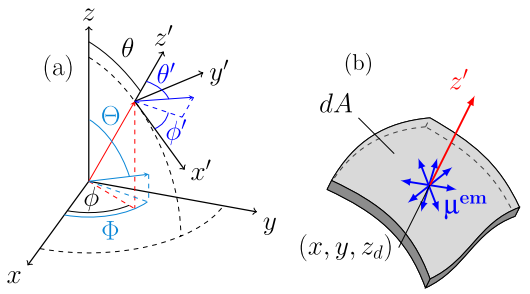

Figure 4. (a) Global and local coordinate systems and (b) schematic illustration of a small section of the cell membrane with its unit normal vector and dipole moments of dil fluorophore.

and layered structure, which is inhomogeneous only in the z-direction, only a portion of the total emitted power reaches on the other side of the structure. The imaging optics focus this power on the image plane, which is situated at a fixed distance from the structure-sample interface. The ratio of collected power at the image plane to total emitted power is denoted as the collection efficiency $Q(z, \boldsymbol{\mu}^{\mathbf{em}})$ of the structure, which depends on the height z of the fluorophore from the planar structure and $\boldsymbol{\mu}^{\mathbf{em}}$. So, the fluorescence power collected at a stationary image plane from a single fluorophore situated at height z from a planar structure is proportional to $|\boldsymbol{\mu}^{\mathbf{ex}} \cdot \mathbf{E}^{\mathbf{ex}}|^2 Q(z, \boldsymbol{\mu}^{\mathbf{em}})$. In the TPCE structure of the proposed technique, we assume that the metal-sample interface is situated at $z = 0$ and the sample is at $z > 0$.

Let us consider a distribution of dipoles, specified by a location- and orientation-dependent concentration $C(z, \Theta, \Phi)$, where Θ and Φ are the zenith and azimuthal angles of the unit emission dipole moment $\boldsymbol{\mu}^{\mathbf{em}}$ in the global coordinate system as shown in figure 4(a). Since the dipoles oscillate incoherently with respect to one another, the total collected fluorescence power due to this distribution of dipoles is an integral of the collected power from individual dipoles. The collected far-field steady-state fluorescence intensity emitted by an ensemble of dipoles from a pixel, which is mathematically defined as a point (x, y), can be written as [69, 70]

$$I(x, y) = k \int_{\Phi=0}^{2\pi} \int_{\Theta=0}^{\pi} \int_{z=0}^{\infty} \mathrm{d}z\mathrm{d}\Omega |\boldsymbol{\mu}^{\mathbf{ex}} \cdot \mathbf{E}^{\mathbf{ex}}|^2 C(z, \Theta, \Phi) Q(z, \boldsymbol{\mu}^{\mathbf{em}}), \quad (1)$$

where $\mathrm{d}\Omega = \sin\Theta \mathrm{d}\Theta \mathrm{d}\Phi$ and k is a pixel-independent constant, which depends on the unit conversion factors and the squared strength of the excitation dipole moment. As intensity is collected pixel-by-pixel, we omit the arguments (x, y) in the mathematical formulation that follows and concentrate on a single pixel.

4.2. Fluorescence from labeled cell membrane

Cell membrane can be mathematically modeled as a surface of arbitrary topography. The orientation of an infinitesimal section of a cell membrane is known if its area normal vector's zenith angle (θ) and azimuthal angle (ϕ) in global coordinate system are known. The local membrane coordinate system has its z'-axis along the membrane area normal, and the x'-axis in the z–z' plane. The global and local coordinate systems for the cell membrane are shown in figure 4(a). The distribution of the fluorophores that are used to label the membrane depends on the local membrane coordinate system. However, to calculate the collected radiation, we need to describe the emission dipole moments in global coordinate system. If the moment of an embedded dipole in a cell membrane is in the direction (θ', ϕ') in the local coordinate system, then the direction of the moment in global coordinate system will be

$$\begin{aligned} \boldsymbol{\mu}^{\mathbf{em}} &= \begin{bmatrix} \boldsymbol{\mu}_x \\ \boldsymbol{\mu}_y \\ \boldsymbol{\mu}_z \end{bmatrix} = \begin{bmatrix} \sin\Theta\cos\Phi \\ \sin\Theta\sin\Phi \\ \cos\Theta \end{bmatrix} \\ &= \begin{bmatrix} \cos\theta\cos\phi & -\sin\phi & \sin\theta\cos\phi \\ \cos\theta\sin\phi & \cos\phi & \sin\theta\sin\phi \\ -\sin\theta & 0 & \cos\theta \end{bmatrix} \\ &\quad \times \begin{bmatrix} \sin\theta'\cos\phi' \\ \sin\theta'\sin\phi' \\ \cos\theta' \end{bmatrix}. \end{aligned} \quad (2)$$

In this work, we neglect the small rotational diffusion between the absorption and emission dipoles and assume that $\boldsymbol{\mu}^{\mathbf{em}} = \boldsymbol{\mu}^{\mathbf{ex}}$ [69].

It has been experimentally found that the emission dipole moments of a number of fluorophores have $\theta' \approx \pi/2$ and ϕ' uniformly distributed in the range $[0, 2\pi]$ when the fluorophores are embedded in the cell membrane, as shown in figure 4(b) [71, 72]. The distribution of the fluorophores in a pixel on the membrane can be written as [69]

$$C(z, \theta', \phi') = C_0 \delta(z - z_d) \delta\left(\theta' - \frac{\pi}{2}\right), \quad (3)$$

where C_0 is a constant, $\delta(\cdot)$ is the Dirac delta function, and z_d is the average height of the membrane in global coordinate system at pixel (x, y). As the distribution of fluorophores in the membrane is known as a function of (z, θ', ϕ') , we convert the variables of integration in equation (1) to θ' and ϕ'. The variables of integration (z, θ', ϕ') and (z, Θ, Φ) are related by the transformations

$$z = z, \quad (4a)$$

$$\Theta = \cos^{-1}(\boldsymbol{\mu}_z), \quad (4b)$$

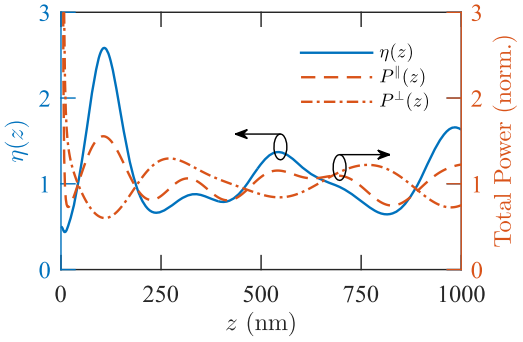

Figure 5. Total power emitted by horizontal and vertical dipoles $P^{\parallel}(z)$ and $P^{\perp}(z)$ in the designed TPCE structure normalized by that of the horizontal and vertical dipoles in free space and their ratio $\eta(z) = P^{\parallel}(z)/P^{\perp}(z)$ with the height of the dipole z from the metal layer.

$$\Phi = \tan^{-1}(\boldsymbol{\mu}_y/\boldsymbol{\mu}_x), \tag{4c}$$

where $\boldsymbol{\mu}_x$, $\boldsymbol{\mu}_y$, and $\boldsymbol{\mu}_z$ can be expressed as functions of θ, θ', ϕ, and ϕ' from equation (2). Therefore, after appropriate substitutions, equation (1) can be written as

$$\begin{aligned} I = k \int_{\phi'=0}^{2\pi} \int_{\theta'=0}^{\pi} \int_{z=0}^{\infty} & \mathrm{d}z\mathrm{d}\theta'\mathrm{d}\phi' \sqrt{\boldsymbol{\mu}_x^2 + \boldsymbol{\mu}_y^2} \\ & \times |J(z, \theta', \phi')| |\boldsymbol{\mu}^{\mathbf{ex}} \cdot \mathbf{E}^{\mathbf{ex}}|^2 \\ & \times C(z, \theta', \phi') Q(z, \boldsymbol{\mu}^{\mathbf{em}}), \end{aligned} \tag{5}$$

where $J(z, \Theta, \Phi; z, \theta', \phi')$ is the Jacobian matrix for the conversion of variables of integration and $\sqrt{\boldsymbol{\mu}_x^2 + \boldsymbol{\mu}_y^2} = \sin\Theta$.

The collection efficiency for the emission of randomly oriented dipoles can be calculated by decomposing and weighting the collection efficiencies of vertically and horizontally oriented dipoles so that [69]

$$\begin{aligned} Q(z, \boldsymbol{\mu}^{\mathbf{em}}) &= \frac{Q^{\perp}(z)}{1 + \eta(z)\tan^2\Theta} \\ &\quad + \frac{Q^{\parallel}(z)}{1 + [\eta(z)\tan^2\Theta]^{-1}} \\ &= \frac{\boldsymbol{\mu}_z^2 Q^{\perp}(z)}{\boldsymbol{\mu}_z^2 + (\boldsymbol{\mu}_x^2 + \boldsymbol{\mu}_y^2)\eta(z)} \\ &\quad + \frac{(\boldsymbol{\mu}_x^2 + \boldsymbol{\mu}_y^2) Q^{\parallel}(z)}{(\boldsymbol{\mu}_x^2 + \boldsymbol{\mu}_y^2) + \boldsymbol{\mu}_z^2[\eta(z)]^{-1}}, \end{aligned} \tag{6}$$

where $Q^{\parallel}(z)$ and $Q^{\perp}(z)$ are the collection efficiencies of parallel and perpendicular dipoles, respectively, and $\eta(z) = P^{\parallel}(z)/P^{\perp}(z)$, where $P^{\parallel}(z)$ and $P^{\perp}(z)$ are the total powers dissipated by dipoles oriented parallel and perpendicular to the interface, respectively [34, 69]. We calculate $P^{\parallel}(z)$ and $P^{\perp}(z)$ for the designed TPCE structure using the mathematical formulation presented in [70]. In figure 5, we show $\eta(z)$, $P^{\parallel}(z)$, and $P^{\perp}(z)$ for the designed TPCE structure. Although the total emitted power from a fluorophore near the metal film, i.e., when $z \approx 0$, is very large, all that power is non-radiatively dissipated as heat in the metal film.

The collected fluorescence can be written as

$$\begin{aligned} I &= kC_0 \int_{\phi'} \int_{\theta'} \int_{z} \mathrm{d}z\mathrm{d}\theta'\mathrm{d}\phi' \sqrt{1 - \boldsymbol{\mu}_z^2} |J(z, \theta', \phi')| \\ &\quad \times |\boldsymbol{\mu}^{\mathbf{ex}} \cdot \mathbf{E}^{\mathbf{ex}}|^2 \delta(z - z_d) \delta\left(\theta' - \frac{\pi}{2}\right) Q(z, \boldsymbol{\mu}^{\mathbf{em}}) \\ &= kC_0 \int_{\phi'} \mathrm{d}\phi' \sqrt{1 - \boldsymbol{\mu}_z^2} |J(z = z_d, \theta' = \pi/2, \phi')| \\ &\quad \times |\boldsymbol{\mu}^{\mathbf{ex}} \cdot \mathbf{E}^{\mathbf{ex}}|^2 Q(z = z_d, \boldsymbol{\mu}^{\mathbf{em}}) \\ &= Q^{\perp}(z_d) f^{\perp}(\theta, \phi, z_d) + Q^{\parallel}(z_d) f^{\parallel}(\theta, \phi, z_d), \end{aligned} \tag{7}$$

where

$$\begin{aligned} f^{\perp}(\theta, \phi, z) &= kC_0 \int_{\phi'} \mathrm{d}\phi' |J(z, \theta' = \pi/2, \phi')| \\ &\quad \times |\boldsymbol{\mu}^{\mathbf{ex}} \cdot \mathbf{E}^{\mathbf{ex}}|^2 \frac{\boldsymbol{\mu}_z^2 \sqrt{1 - \boldsymbol{\mu}_z^2}}{\boldsymbol{\mu}_z^2 + (\boldsymbol{\mu}_x^2 + \boldsymbol{\mu}_y^2)\eta(z)}, \end{aligned} \tag{8a}$$

$$\begin{aligned} f^{\parallel}(\theta, \phi, z) &= kC_0 \int_{\phi'} \mathrm{d}\phi' |J(z, \theta' = \pi/2, \phi')| \\ &\quad \times |\boldsymbol{\mu}^{\mathbf{ex}} \cdot \mathbf{E}^{\mathbf{ex}}|^2 \frac{(\boldsymbol{\mu}_x^2 + \boldsymbol{\mu}_y^2)\sqrt{1 - \boldsymbol{\mu}_z^2}}{(\boldsymbol{\mu}_x^2 + \boldsymbol{\mu}_y^2) + \boldsymbol{\mu}_z^2[\eta(z)]^{-1}}. \end{aligned} \tag{8b}$$

The weighting functions $f^{\perp}(\theta, \phi, z)$ and $f^{\parallel}(\theta, \phi, z)$ depend on the polarization of the excitation field, and position and orientation of the membrane. The weighting functions represent the amount of horizontal and vertical dipoles excited by the excitation light $\mathbf{E}^{\mathbf{ex}}$. We will note that z and θ' are replaced by z_d and $\pi/2$, respectively, in equation (7).

4.3. *P*-polarized excitation

If p-polarized excitation light with a constant amplitude E_0 is incident from the substrate at an angle θ_p, which is greater than the critical angle $\sin^{-1}(n_c/n_s)$, in the x–z plane, then the wavevector in the sample region can be written as

$$\begin{aligned} \mathbf{k} = k_x \hat{\mathbf{x}} + jk_z \hat{\mathbf{z}} = k_0 [n_s \sin\theta_p \hat{\mathbf{x}} \\ + j\sqrt{n_s^2 \sin^2\theta_p - n_c^2}\, \hat{\mathbf{z}}], \end{aligned} \tag{9}$$

where k_0 is the free space wavevector, and n_s and n_c are the refractive indices of substrate and sample layers, respectively. The imaginary factor j with k_z denotes the evanescent nature of the excitation field inside the sample layer. Maxwell's equation in Fourier space requires $\mathbf{k} \cdot \mathbf{E}^{\mathbf{ex}} = 0$, where $\mathbf{E}^{\mathbf{ex}}$ is the phasor of the excitation electric field. Therefore,

$$k_x E_x + jk_z E_z = 0, \tag{10}$$

where E_x and E_z are the x and z components of the phasor of excitation electric field. Equation (10) yields

$$\frac{E_x}{E_z} = -j\frac{k_z}{k_x} = \frac{\sqrt{n_s^2 \sin^2\theta_p - n_c^2}}{jn_s \sin\theta_p}, \tag{11}$$

which means that there is a quadrature phase delay between x and z components of the excitation field as

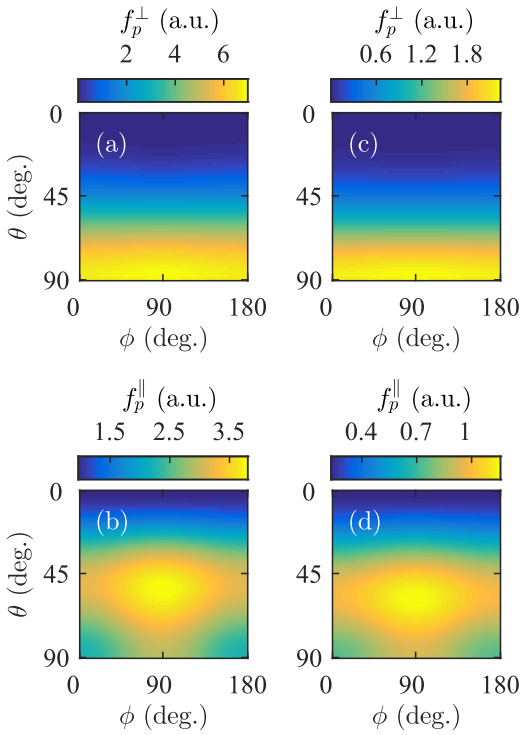

Figure 6. Weighting functions (a) $f_p^{\perp}$ and (b) $f_p^{\parallel}$ at $z = 40$ nm, where $\eta = 1$, and weighting functions (c) $f_p^{\perp}$ and (d) $f_p^{\parallel}$ at $z = 140$ nm, where $\eta = 2$.

the evanescent field created by *p*-polarized light is elliptically polarized [73, 74]. Therefore, the excitation field can be written as

$$\mathbf{E}^{\mathbf{ex}} = E_0|t_p|n_s(\hat{\mathbf{x}}\sqrt{\sin^2\theta_p - (n_c/n_s)^2} + j\hat{\mathbf{z}}\sin\theta_p)\exp(-z/2d_p), \quad (12)$$

where t_p is the Fresnel transmission coefficient of the structure from glass side, and $d_p = (\lambda/4\pi)\sqrt{n_s^2\sin^2(\theta_p) - n_c^2}$ is the penetration depth of the *p*-polarized electric field inside the sample. Therefore, the excitation probability of fluorophores can be written as

$$|\boldsymbol{\mu}^{\mathbf{ex}}\cdot\mathbf{E}^{\mathbf{ex}}|^2 \propto [|\boldsymbol{\mu}_x|^2(\sin^2\theta_p - (n_c/n_s)^2) + |\boldsymbol{\mu}_z|^2\sin^2\theta_p]\exp(-z/d_p), \quad (13)$$

since E_0, t_p, and n_s are constants. By substituting $|\boldsymbol{\mu}^{\mathbf{ex}}\cdot\mathbf{E}^{\mathbf{ex}}|^2$ in equations (8*a*) and (8*b*) by the expression in equation (13), we get the weighting functions $f_p^{\perp}$ and $f_p^{\parallel}$ for *p*-polarized excitation. The weighting functions $f_p^{\perp}$ and $f_p^{\parallel}$ represent the effective amount of vertical and horizontal dipoles excited by *p*-polarized light and they are functions of the orientation of membrane (θ, ϕ), height of the membrane *z*, and the incidence angle θ_p of excitation light. In figures 6(a) and (b), we show $f_p^{\perp}$ and $f_p^{\parallel}$ against θ and ϕ at $z = 40$ nm, where $\eta = 1$. We note that the amount of effective horizontal and vertical dipoles excited depends on the orientation of membrane. In figures 6(c) and (d), we show $f_p^{\perp}$ and $f_p^{\parallel}$ at $z = 140$ nm, where $\eta = 2$. The weighting functions decrease exponentially with height *z*.

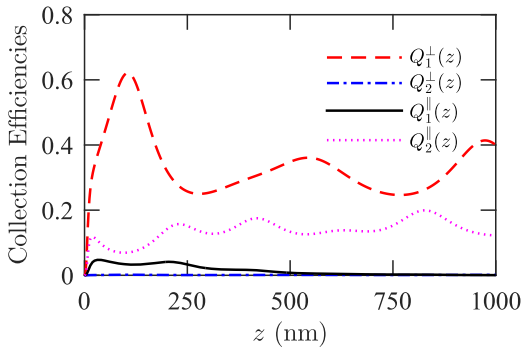

Figure 7. Collection efficiencies of the designed TPCE structure at θ_1 and θ_2 angle for different orientations of the dipoles.

The *p*-polarized excitation will cause the fluorophores to emit light, which will come out of the glass substrate in two reflectance minima angles θ_1 and θ_2. If we refer fluorescence intensities collected around θ_1 and θ_2 as I_1 and I_2, respectively, we can write

$$I_1^p = k'[Q_1^{\parallel}(z_d)f_p^{\parallel}(\theta, \phi, z_d) + Q_1^{\perp}(z_d)f_p^{\perp}(\theta, \phi, z_d)], \quad (14a)$$

$$I_2^p = k'[Q_2^{\parallel}(z_d)f_p^{\parallel}(\theta, \phi, z_d) + Q_2^{\perp}(z_d)f_p^{\perp}(\theta, \phi, z_d)]. \quad (14b)$$

The collection efficiencies $Q_{1,2}^{\perp,\parallel}(z)$ are shown in figure 7. The collection efficiencies $Q_1^{\perp,\parallel}(z)$ ($Q_2^{\perp,\parallel}(z)$) represent the power collected around the collection angle θ_1 (θ_2) for vertical and horizontal dipoles, respectively, situated at a height *z*. As the emission from a vertical dipole is *p*-polarized, the collection efficiency for a vertical dipole at the *s*-polarized emission angle θ_2 is very small compared to that at the *p*-polarized emission angle θ_1, i.e., $Q_1^{\perp}(z) \gg Q_2^{\perp}(z)$. Also, the *p*-polarized emission from a horizontal dipole is very small, i.e., $Q_2^{\parallel}(z) \gg Q_1^{\parallel}(z)$. These approximations can be used to simplify equation (14) for an intuitive understanding of the obtained images. Therefore, using these approximations, we can write the fluorescence intensities as

$$I_1^p \approx k'Q_1^{\perp}f_p^{\perp}, \quad (15a)$$

$$I_2^p \approx k'Q_2^{\parallel}f_p^{\parallel}. \quad (15b)$$

The ratio of the two intensities in equation (15) can be written as

$$\frac{I_1^p}{I_2^p} \approx \frac{Q_1^{\perp}f_p^{\perp}}{Q_2^{\parallel}f_p^{\parallel}}. \quad (16)$$

The orientation-dependence of I_1^p/I_2^p comes mainly from $f_p^{\perp}/f_p^{\parallel}$. In figure 8, we show $f_p^{\perp}/f_p^{\parallel}$ at $z = 40$ nm. We note that $f_p^{\perp}/f_p^{\parallel}$ is not very sensitive to the change in ϕ. However, $f_p^{\perp}/f_p^{\parallel}$ increases steadily with the increase of θ. Therefore, the ratio image of

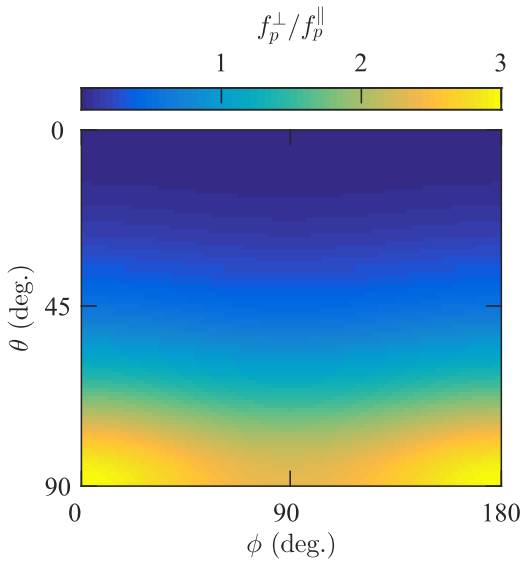

Figure 8. Ratio of perpendicular to horizontal weighting functions of p-polarized excitation for $\theta_p = 66.8°$ and $z = 40$ nm.

I_1^p/I_2^p will have large values in the pixels where the membrane normal is perpendicular to the global z-axis.

4.4. *S*-polarized excitation

If s-polarized light incident at θ_s excites the fluorophores, the excitation probability will be

$$|\boldsymbol{\mu}^{\mathbf{ex}} \cdot \mathbf{E}^{\mathbf{ex}}|^2 \propto |\boldsymbol{\mu}_y|^2 \exp(-z/d_s), \tag{17}$$

where $d_s = (\lambda/4\pi)\sqrt{n_s^2 \sin^2(\theta_s) - n_c^2}$ is the penetration depth of the s-polarized electric field. For s-polarized excitation, the collected fluorescence intensities can be written as

$$I_1^s = k'[Q_1^{\parallel}(z_d) f_s^{\parallel}(\theta, \phi, z_d) + Q_1^{\perp}(z_d) f_s^{\perp}(\theta, \phi, z_d)], \tag{18a}$$

$$I_2^s = k'[Q_2^{\parallel}(z_d) f_s^{\parallel}(\theta, \phi, z_d) + Q_2^{\perp}(z_d) f_s^{\perp}(\theta, \phi, z_d)], \tag{18b}$$

where $f_s^{\perp}$ and $f_s^{\parallel}$ are the effective amount of vertical and horizontal dipoles excited by s-polarized light. In figures 9(a) and (b), we show $f_s^{\perp}$ and $f_s^{\parallel}$ against θ and ϕ at $z = 40$ nm, where $\eta = 1$. In figures 9(c) and (d), we show $f_s^{\perp}$ and $f_s^{\parallel}$ at $z = 140$ nm, where $\eta = 2$. We note that $f_s^{\perp}$ and $f_s^{\parallel}$ decrease exponentially with respect to the height of the dipole z on the cell membrane. Using the same approximations of the collection efficiencies that have been used for p-polarized excitation, the collected intensities for s-polarized excitation can be simplified for an intuitive understanding as

$$I_1^s \approx k' Q_1^{\perp} f_s^{\perp}, \tag{19a}$$

$$I_2^s \approx k' Q_2^{\parallel} f_s^{\parallel}. \tag{19b}$$

Therefore, the ratio of the two intensities in equation (19) can be written as

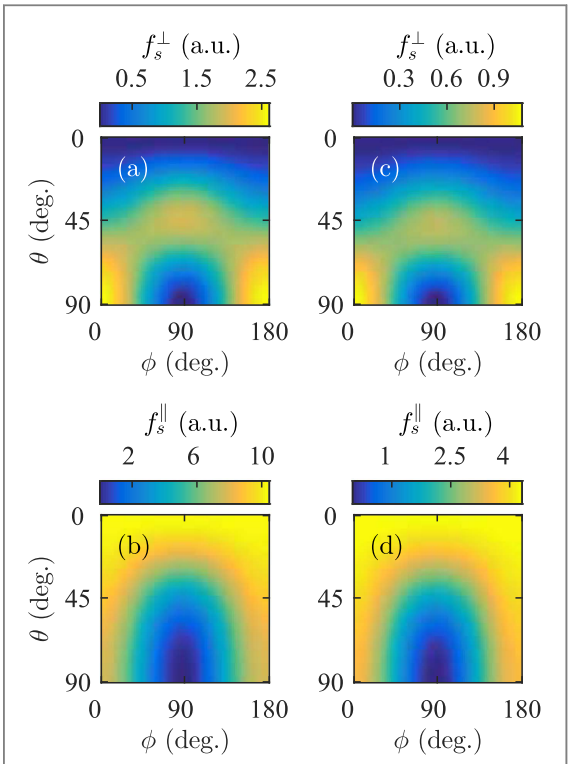

Figure 9. Weighting functions (a) $f_s^{\perp}$ and (b) $f_s^{\parallel}$ at $z = 40$ nm, where $\eta = 1$, and weighting functions (c) $f_s^{\perp}$ and (d) $f_s^{\parallel}$ at $z = 140$ nm, where $\eta = 2$.

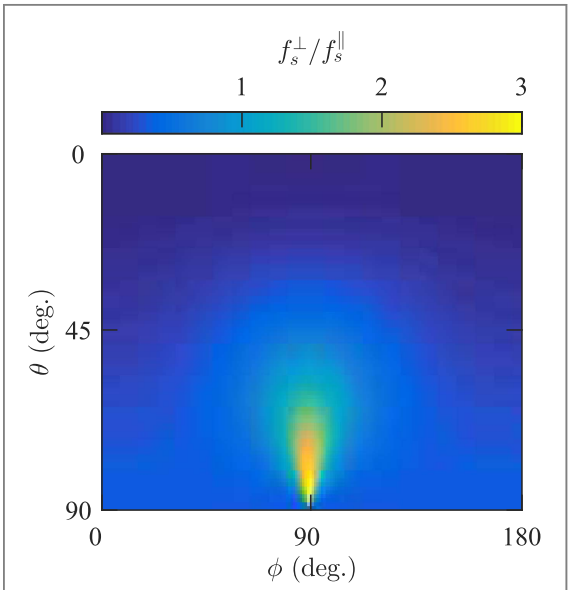

Figure 10. Ratio of perpendicular to horizontal weighting functions of s-polarized excitation for $\theta_s = 63.7°$ and $z = 40$ nm.

$$\frac{I_1^s}{I_2^s} \approx \frac{Q_1^{\perp} f_s^{\perp}}{Q_2^{\parallel} f_s^{\parallel}}. \tag{20}$$

In figure 10, we show the ratio $f_s^{\perp}/f_s^{\parallel}$ against θ and ϕ, where $z = 40$ nm. For smaller values of θ, $f_s^{\perp}/f_s^{\parallel}$ does not depend on ϕ. For a pixel on the membrane with a small θ ϕ, $f_s^{\perp}/f_s^{\parallel}$ carries no new information. However, for large values of θ, we find that $f_s^{\perp}/f_s^{\parallel}$ has a

strong dependence on ϕ and provides information about the orientation of the membrane.

5. Imaging procedure

In this section, we summarize the steps required for imaging the cell membrane topography using the proposed TPCE-based scheme as follows:

Step 1: The sample is excited with p-polarized light incident at the p-polarized reflectance minimum angle θ_p. The fluorophore labels of the sample radiate and TPCE at the substrate side occurs at two angles θ_1 and θ_2. The images that result from the collection of fluorescence intensity around θ_1 and θ_2, i.e., I_1^p and I_2^p, are captured separately.

Step 2: The ratio image I_1^p/I_2^p is calculated pixel-by-pixel. The ratio image I_1^p/I_2^p will have a high value at pixels where the membrane-normal direction is perpendicular to the global z-axis and a low value where the membrane-normal direction is parallel to the global z-axis.

Step 3: The sample is then excited with s-polarized light incident at the s-polarized reflectance minimum angle θ_s. The fluorophore labels of the sample radiate and TPCE at substrate side occurs at two angles θ_1 and θ_2. The images that result from the collection of fluorescence intensity around θ_1 and θ_2, i.e., I_1^s and I_2^s, are captured separately.

Step 4: The ratio image I_1^s/I_2^s is calculated pixel-by-pixel. The ratio image I_1^s/I_2^s will have a high value at pixels where the membrane area vector is azimuthally normal with the incident x–z plane and is normal to the global z axis.

6. Image of a membrane

We now calculate images of a hypothetical diI-labeled plasma membrane using the developed mathematical models given in equations (14) and (18) when the proposed and pTIRFM techniques are applied. We assume that a sample of fluorescently labeled membrane is fusing a spherical granule that has a radius of 150 nm. The topography of the sample cell membrane, i.e., the distance of the membrane from the metal layer is shown in figure 11. Three regions of the membrane, named A, B and C, are selected and marked with rectangles in figure 11. The respective values of membrane-normal angles (θ, ϕ) at the center of the rectangle in these regions are given in table 2. Although, in practice, the point spread function (PSF) of the imaging optics will be much broader, we assume the PSF to be a Dirac impulse function $\delta(x, y)$ in our calculation for the proposed and pTIRFM techniques [55]. The images captured with a broad PSF can be calculated by two-dimensional convolution of the images obtained in this work with the actual PSF.

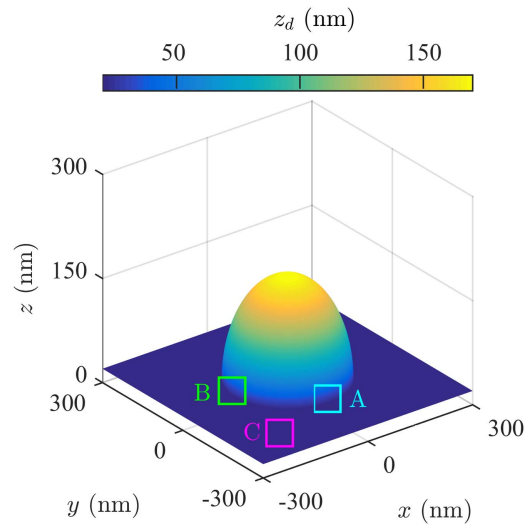

Figure 11. Cell membrane topography during invagination of a spherical granule.

Table 2. θ and ϕ in regions A, B and C.

Region	θ (rad.)	ϕ (rad.)
A	$\pi/2$	$-\pi/2$
B	$\pi/2$	π
C	0	0

In figure 12, we show the calculated images obtained from steps 1 and 2 of the imaging procedure. The parts of the image that are from regions A, B, and C of the membrane are marked with same color-coded rectangles as in figure 11. We note that I_1^p shows peak values at regions where the membrane-normal direction is perpendicular to the z-axis, as we find in regions A and B. We also note that I_2^p has a relatively high value in region C, where the membrane normal is in the z-direction and all the dipoles have horizontal moments. As expected from figure 6, images obtained by p-polarized excitation provide θ information, but do not show noticeable change with ϕ, which is evident from the comparison of regions A and B in the image. The ratio image I_1^p/I_2^p is shown in figure 12(c), which reaches maximum at positions where $\theta = \pi/2$, such as in regions A and B.

We show the calculated images obtained from steps 3 and 4 in figure 13. We note that, although regions A and B both have $\theta = \pi/2$, they show different I_1^s and I_2^s values due to their different ϕ values as given in table 2. Therefore, images captured by s-polarized excitation provide information about the ϕ-orientation of the cell membrane. Also, s-polarized excitation light only excites dipoles with horizontal moment. Therefore, I_1^s and I_2^s have a small value in region A, where the dipole moments are oriented in the x–z plane. The image intensity I_2^s at region C is very

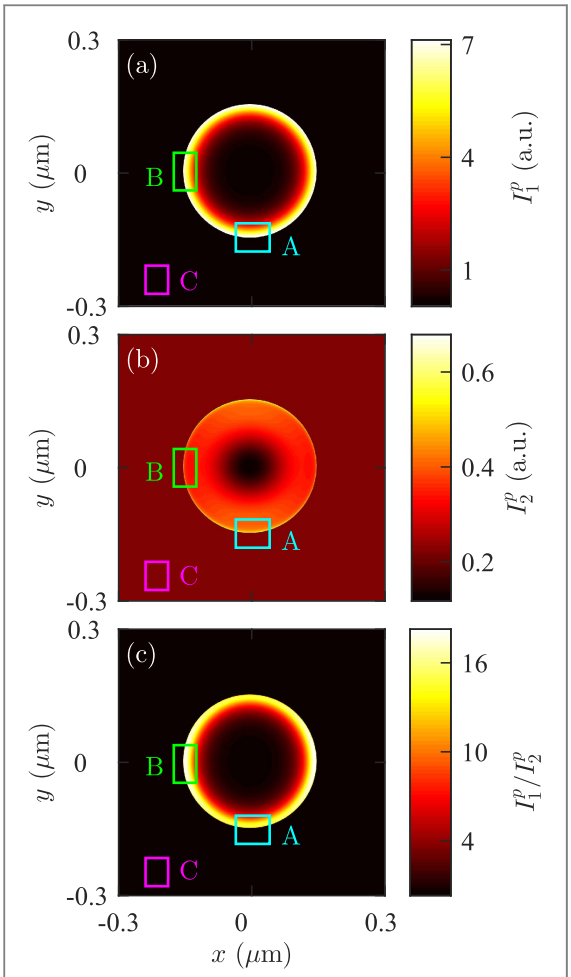

Figure 12. Calculated images of the cell membrane for *p*-polarized excitation light using the proposed technique (a) collected around θ_1, i.e., I_1^p, (b) collected around θ_2, i.e., I_2^p, and (c) the ratio of these two images, i.e., I_1^p/I_2^p.

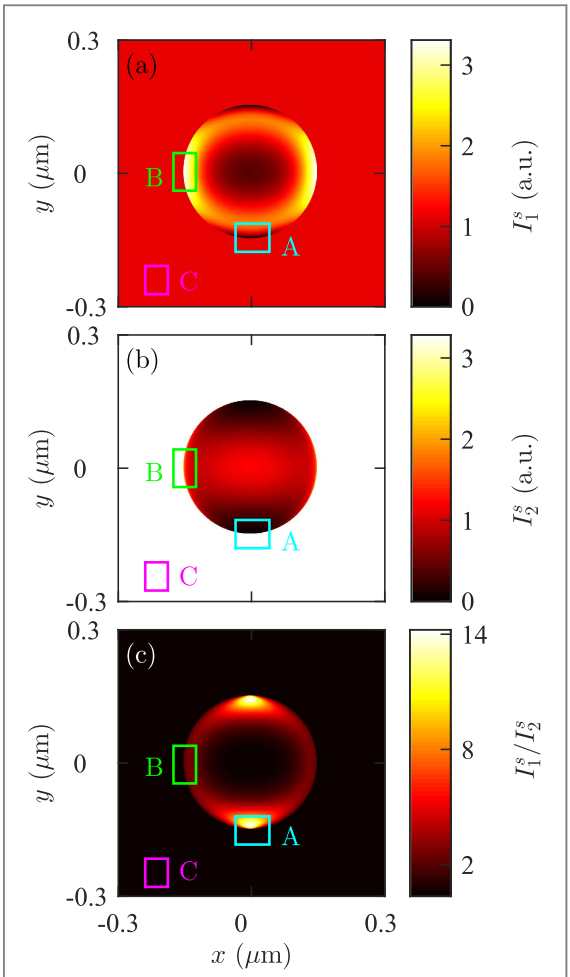

Figure 13. Calculated images of the cell membrane for *s*-polarized excitation light using the proposed technique (a) collected around θ_1, i.e., I_1^s, (b) collected around θ_2, i.e., I_2^s, and (c) the ratio of these two images, i.e., I_1^s/I_2^s.

high due to *s*-polarized excitation of horizontal dipoles. The ratio image I_1^s/I_2^s reaches maximum at region A, where $\theta = \pi/2$ and $\phi = \pi/2$, as expected from figure 10. Although $\theta = \pi/2$ at region B, the intensity is low as $\phi = \pi$.

In figure 14, we show the calculated images obtained by using a pTIRFM technique, where the sample is directly placed on the top of a plane glass substrate. Typical TIRFM structures do not emit radiation sharply in one direction but over a broad range of angles. Therefore, an image is collected for an excitation by focusing the total radiation toward the image plane. Figures 14(a) and (b) show the images that are created for *p*- and *s*-polarized excitations. The ratio of the images is shown in figure 14(c). We note that the calculated images are similar to the ones given in [23]. The θ and ϕ information is convoluted in the ratio image. We note that I_t^p shows only θ dependence, as evident by the approximately equal values at regions A and B.

We note that the dynamic range of the ratio images obtained by the proposed method, as shown in figures 12(c) and 13(c), is ~10 times greater than the ratio image obtained by the conventional pTIRFM technique, as shown in figure 14(c). The reason behind this is that the contribution of horizontal and vertical dipoles are both present in images of figures 14(a) and (b). By contrast, they are isolated in the proposed method, which is obvious if we compare the backgrounds in figures 12(a) and 14(a).

To quantitatively assess the quality of the image obtained by the proposed technique with that obtained by a pTIRFM technique, we calculate the SSIM of the images with respect to a reference image. SSIM is a widely used metric in digital image processing for similarity comparison between images [75]. SSIM assesses the visual impact of changes in image luminance, contrast, and structure between an image and a reference image regarded as of perfect quality [76]. We create two images $I_\theta(x, y)$ and $I_\phi(x, y)$ in figure 15 for the membrane in figure 11. The images $I_\theta(x, y)$ and $I_\phi(x, y)$ contain values of θ and $|\phi|$ at each pixel (x, y). We calculate SSIM of the images obtained by the proposed and pTIRFM techniques taking $I_\theta(x, y)$ and $I_\phi(x, y)$ as references. We present the maximum SSIM index values from each techniques in table 3. The SSIM between two images can have a maximum value of 1, which means 100% structural match

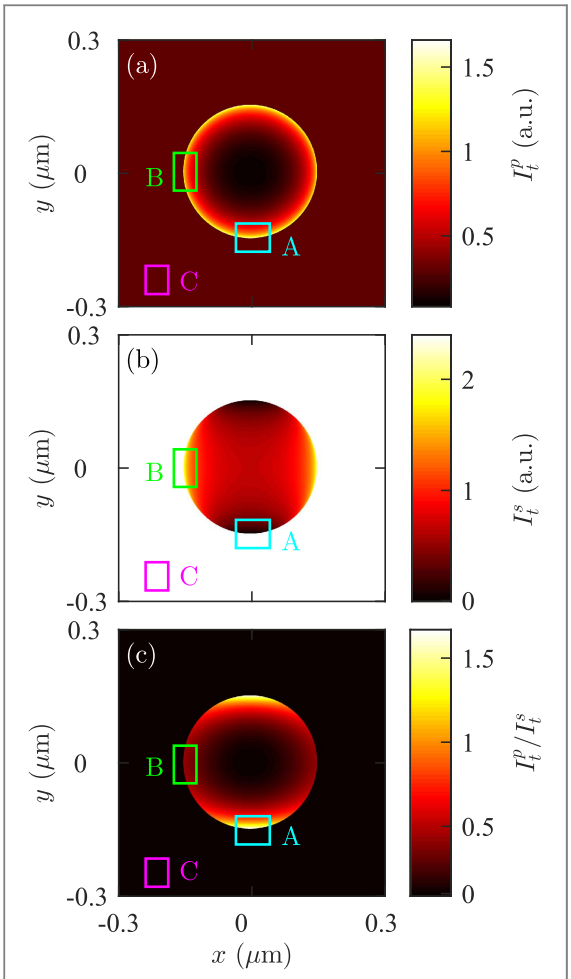

Figure 14. Calculated images of the cell membrane using a pTIRFM technique in (a) *p*-polarized excitation, i.e., I_t^p, (b) *s*-polarized excitation, i.e., I_t^s, and (c) *p*/*s*-ratio of the image, i.e., I_t^p/I_t^s.

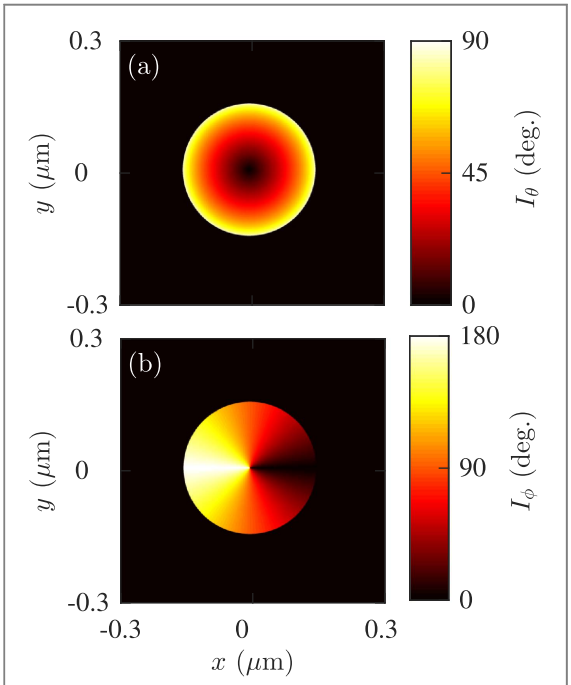

Figure 15. Values of (a) θ and (b) ϕ at various pixels of the granule invaginating membrane.

Table 3. Maximum SSIM for proposed method and pTIRFM.

Technique	$SSIM_{I_\theta}$	$SSIM_{I_\phi}$
Proposed	0.7720	0.7303
pTIRFM	0.1610	0.1075

between the images. The I_1^p image acquired by the proposed method shows ~77% match with I_θ, and thus, successfully extracts the θ information of the membrane, whereas the pTIRFM technique shows a maximum ~16% match with I_θ. Similarly, the proposed technique shows a maximum ~73% match with I_ϕ, whereas the pTIRFM technique shows a maximum ~10% match with I_ϕ.

7. Conclusion

A clear image of the cell membrane topography is important to understand a cell's interactions with its environment, which is fundamental to most activities in a living organism. An image of the cell membrane topography with a better contrast ratio with respect to the background than that already available using pTIRFM will enable us to interpret the details of the biological phenomena that cause a change in the topography of the cell membrane with greater accuracy. We proposed a new microscopy technique based on TPCE, where the cell membrane is placed on a metal layer, which is attached to a one-dimensional photonic crystal. We showed that by appropriately designing the one-dimensional photonic crystal, the sample can be excited separately by *p*- and *s*-polarized incident light. The one-dimensional photonic crystal can also be designed to collect the radiation of the vertically and horizontally oriented fluorophores separately. Polarization-specific excitation of the sample and orientation-dependent collection of the radiated fluorescence help to create an image of the sample that has a greater contrast ratio with respect to the background noise than that of the image created using a pTIRFM technique. The image created using the proposed technique also shows a greater SSIM with a reference image, when compared to that using a pTIRFM technique.

Appendix. Determinant of the Jacobian Matrix

The Jacobian matrix is defined as

$$J(z,\theta',\phi') = \begin{bmatrix} \frac{\partial z}{\partial z} & \frac{\partial \Theta}{\partial z} & \frac{\partial \Phi}{\partial z} \\ \frac{\partial z}{\partial \theta'} & \frac{\partial \Theta}{\partial \theta'} & \frac{\partial \Phi}{\partial \theta'} \\ \frac{\partial z}{\partial \phi'} & \frac{\partial \Theta}{\partial \phi'} & \frac{\partial \Phi}{\partial \phi'} \end{bmatrix}. \quad (21)$$

From the transformation relations between (h, θ', ϕ') and (h, Θ, Φ), the required derivatives for evaluating

the Jacobian matrix can be written as

$$\frac{\partial z}{\partial z} = 1, \tag{22a}$$

$$\frac{\partial \Theta}{\partial z} = 0, \tag{22b}$$

$$\frac{\partial \Phi}{\partial z} = 0, \tag{22c}$$

$$\frac{\partial z}{\partial \theta'} = 0, \tag{22d}$$

$$\frac{\partial \Theta}{\partial \theta'} = -\frac{1}{\sin\Theta}\frac{\partial \boldsymbol{\mu}_z}{\partial \theta'} = -\frac{1}{\sqrt{1-\boldsymbol{\mu}_z^2}}\frac{\partial \boldsymbol{\mu}_z}{\partial \theta'}, \tag{22e}$$

$$\frac{\partial \Phi}{\partial \theta'} = \cos^2\Phi\frac{\partial}{\partial \theta'}\left(\frac{\boldsymbol{\mu}_y}{\boldsymbol{\mu}_x}\right) = \frac{\boldsymbol{\mu}_x^2}{\boldsymbol{\mu}_x^2+\boldsymbol{\mu}_y^2}\frac{\partial}{\partial \theta'}\left(\frac{\boldsymbol{\mu}_y}{\boldsymbol{\mu}_x}\right), \tag{22f}$$

$$\frac{\partial z}{\partial \phi'} = 0, \tag{22g}$$

$$\frac{\partial \Theta}{\partial \phi'} = -\frac{1}{\sqrt{1-\boldsymbol{\mu}_z^2}}\frac{\partial \boldsymbol{\mu}_z}{\partial \phi'}, \tag{22h}$$

$$\frac{\partial \Phi}{\partial \phi'} = \frac{\boldsymbol{\mu}_x^2}{\boldsymbol{\mu}_x^2+\boldsymbol{\mu}_y^2}\frac{\partial}{\partial \phi'}\left(\frac{\boldsymbol{\mu}_y}{\boldsymbol{\mu}_x}\right). \tag{22i}$$

The explicit expressions of $\boldsymbol{\mu}_{x,y,z}$ as a function of $(\theta,\ \phi,\ \theta',\ \phi')$ can be written as

$$\boldsymbol{\mu}_x = \cos(\phi)\cos(\theta')\sin(\theta) - \sin(\phi)\sin(\phi')\sin(\theta') + \cos(\phi)\cos(\phi')\cos(\theta)\sin(\theta'), \tag{23a}$$

$$\boldsymbol{\mu}_y = \cos(\theta')\sin(\phi)\sin(\theta) + \cos(\phi)\sin(\phi')\sin(\theta') + \cos(\phi')\cos(\theta)\sin(\phi)\sin(\theta'), \tag{23b}$$

$$\boldsymbol{\mu}_z = \cos(\theta')\cos(\theta) - \cos(\phi')\sin(\theta')\sin(\theta). \tag{23c}$$

The expressions of $\boldsymbol{\mu}_{x,y,z}$ in equations (23*a*)–(23*c*) can be used to calculate the derivatives, and hence find the determinant of the Jacobian matrix.

ORCID iDs

Muhammad Anisuzzaman Talukder https://orcid.org/0000-0002-2814-3658

References

[1] Parmryd I and Önfelt B 2013 Consequences of membrane topography *Fed. Eur. Biochem. Soc. J.* **280** 2775–84

[2] Murase K *et al* 2004 Ultrafine membrane compartments for molecular diffusion as revealed by single molecule techniques *Biophys. J.* **86** 4075–93

[3] Wu E-S, Tank D W and Webb W W 1982 Unconstrained lateral diffusion of concanavalin a receptors on bulbous lymphocytes *Proc. Natl Acad. Sci.* **79** 4962–6

[4] Steyer J A and Almers W 2001 A real-time view of life within 100 nm of the plasma membrane *Nat. Rev. Mol. Cell Biol.* **2** 268–75

[5] McNeil P L and Steinhardt R A 2003 Plasma membrane disruption: repair, prevention, adaptation *Annu. Rev. Cell Dev. Biol.* **19** 697–731

[6] Reddy A, Caler E V and Andrews N W 2001 Plasma membrane repair is mediated by Ca^{2+}-regulated exocytosis of lysosomes *Cell* **106** 157–69

[7] Ridley A J 2011 Life at the leading edge *Cell* **145** 1012–22

[8] Petrie R J and Yamada K M 2012 At the leading edge of three-dimensional cell migration *J. Cell Sci.* **125** 5917–26

[9] Keren K 2011 Cell motility: the integrating role of the plasma membrane *Eur. Biophys. J.* **40** 1013–27

[10] Paluch E K and Raz E 2013 The role and regulation of blebs in cell migration *Curr. Opin. Cell Biol.* **25** 582–90

[11] Henderson R and Unwin P N T 1975 Three-dimensional model of purple membrane obtained by electron microscopy *Nature* **257** 28–32

[12] Schoenenberger C-A and Hoh J 1994 Slow cellular dynamics in MDCK and R5 cells monitored by time-lapse atomic force microscopy *Biophys. J.* **67** 929

[13] Girasole M *et al* 2007 Roughness of the plasma membrane as an independent morphological parameter to study RBCs: a quantitative atomic force microscopy investigation *Biochim. Biophys. Acta (BBA)-Biomembr.* **1768** 1268–76

[14] Korchev Y E *et al* 1997 Scanning ion conductance microscopy of living cells *Biophys. J.* **73** 653

[15] Verschueren H 1985 Interference reflection microscopy in cell biology: Methodology and applications *J. Cell Sci.* **75** 279–301

[16] Owen D M *et al* 2012 Optical techniques for imaging membrane domains in live cells (live-cell palm of protein clustering) *Methods Enzymol.* **504** 221–35

[17] Thompson R F *et al* 2016 An introduction to sample preparation and imaging by cryo-electron microscopy for structural biology *Methods* **100** 3–15

[18] Betz W J, Mao F and Smith C B 1996 Imaging exocytosis and endocytosis *Curr. Opin. Neurobiol.* **6** 365–71

[19] Sund S E, Swanson J A and Axelrod D 1999 Cell membrane orientation visualized by polarized total internal reflection fluorescence *Biophys. J.* **77** 2266–83

[20] Mattheyses A L, Simon S M and Rappoport J Z 2010 Imaging with total internal reflection fluorescence microscopy for the cell biologist *J. Cell Sci.* **123** 3621–8

[21] Johnson D S, Jaiswal J K and Simon S 2012 Total internal reflection fluorescence (TIRF) microscopy illuminator for improved imaging of cell surface events *Curr. Protocols Cytometry* **61** 12–29

[22] Kress A *et al* 2013 Mapping the local organization of cell membranes using excitation-polarization-resolved confocal fluorescence microscopy *Biophys. J.* **105** 127–36

[23] Anantharam A *et al* 2010 Localized topological changes of the plasma membrane upon exocytosis visualized by polarized tirfm *J. Cell Biol.* **188** 415–28

[24] Enderlein J 1999 Single-molecule fluorescence near a metal layer *Chem. Phys.* **247** 1–9

[25] Stefani F *et al* 2005 Surface-plasmon-mediated single-molecule fluorescence through a thin metallic film *Phys. Rev. Lett.* **94** 023005

[26] Hiep H M, Fujii M and Hayashi S 2007 Effects of molecular orientation on surface-plasmon-coupled emission patterns *Appl. Phys. Lett.* **91** 183110

[27] Benner R E, Dornhaus R and Chang R K 1979 Angular emission profiles of dye molecules excited by surface plasmon waves at a metal surface *Opt. Commun.* **30** 145–9

[28] Lakowicz J R *et al* 2003 Directional surface plasmon-coupled emission: a new method for high sensitivity detection *Biochem. Biophys. Res. Commun.* **307** 435–9

[29] Lakowicz J R 2004 Radiative decay engineering 3. surface plasmon-coupled directional emission *Anal. Biochem.* **324** 153–69

[30] Gryczynski I *et al* 2004 Radiative decay engineering 4. experimental studies of surface plasmon-coupled directional emission *Anal. Biochem.* **324** 170–82

[31] Lakowicz J R 2005 Radiative decay dngineering 5: Metal-enhanced fluorescence and plasmon emission *Anal. Biochem.* **337** 171–94

[32] Calander N 2004 Theory and simulation of surface plasmon-coupled directional emission from fluorophores at planar structures *Anal. Chem.* **76** 2168–73
[33] Calander N 2005 Surface plasmon-coupled emission and fabry-perot resonance in the sample layer: a theoretical approach *J. Phys. Chem.* B **109** 13957–63
[34] Enderlein J and Ruckstuhl T 2005 The efficiency of surface-plasmon coupled emission for sensitive fluorescence detection *Opt. Express* **13** 8855–65
[35] Ray K *et al* 2007 Distance dependence of surface plasmon-coupled emission observed using Langmuir–Blodgett films *Appl. Phys. Lett.* **90** 251116
[36] Gryczynski Z *et al* 2006 Minimization of detection volume by surface-plasmon-coupled emission *Anal. Biochem.* **356** 125–31
[37] Borejdo J *et al* 2006 Application of surface plasmon coupled emission to study of muscle *Biophys. J.* **91** 2626–35
[38] Toma K *et al* 2013 Compact surface plasmon-enhanced fluorescence biochip *Opt. Express* **21** 10121–32
[39] Uddin S Z, Tanvir M R and Talukder M A 2016 A proposal and a theoretical analysis of an enhanced surface plasmon coupled emission structure for single molecule detection *J. Appl. Phys.* **119** 204701
[40] Maier S A 2007 *Plasmonics: Fundamentals and Applications* (New York: Springer Science & Business Media)
[41] Badugu R, Descrovi E and Lakowicz J R 2014 Radiative decay engineering 7: Tamm state-coupled emission using a hybrid plasmonic-photonic structure *Anal. Biochem.* **445** 1–13
[42] Chen Y *et al* 2014 Tamm plasmon and surface plasmon-coupled emission from hybrid plasmonic-photonic structures *Optica* **1** 407–13
[43] Chen Y *et al* 2014 Back focal plane imaging of tamm plasmons and their coupled emission *Laser Photonics Rev.* **8** 933–40
[44] Badugu R and Lakowicz J R 2014 Tamm state-coupled emission: effect of probe location and emission wavelength *J. Phys. Chem.* C **118** 21558–71
[45] Dutta Choudhury S, Badugu R and Lakowicz J R 2015 Directing fluorescence with plasmonic and photonic structures *Acc. Chem. Res.* **48** 2171–80
[46] Fang Y-T *et al* 2013 Surface waves with near-zero or negative group velocity on one-dimensional photonic crystal coated with one metal film *Opt. Commun.* **298–299** 129–34
[47] Gryczynski I *et al* 2004 Effects of sample thickness on the optical properties of surface plasmon-coupled emission *J. Phys. Chem.* B **108** 12073–83
[48] Gingell D, Heavens O and Mellor J 1987 General electromagnetic theory of total internal reflection fluorescence: the quantitative basis for mapping cell-substratum topography *J. Cell Sci.* **87** 677–93 http://jcs.biologists.org/content/87/5/677
[49] Rosen R 2013 *Optimality Principles in Biology* (Berlin: Springer)
[50] Reichert W and Truskey G 1990 Total internal reflection fluorescence (TIRF) microscopy: I. Modelling cell contact region fluorescence *J. Cell Sci.* **96** 219–30 http://jcs.biologists.org/content/87/5/677
[51] Stock K *et al* 2003 Variable-angle total internal reflection fluorescence microscopy (VA-TIRFM): realization and application of a compact illumination device *J. Microsc.* **211** 19–29
[52] Berreman D W 1972 Optics in stratified and anisotropic media: 4 × 4-matrix formulation *J. Opt. Soc. Am.* **62** 502–10
[53] Yeh P 1980 Optics of anisotropic layered media: a new 4 × 4 matrix algebra *Surf. Sci.* **96** 41–53
[54] Schubert M 1996 Polarization-dependent optical parameters of arbitrarily anisotropic homogeneous layered systems *Phys. Rev.* B **53** 4265
[55] Gryczynski Z *et al* 2007 New surface plasmons approach to single molecule detection (SMD) and fluorescence correlation spectroscopy (FCS) *Biomedical Optics (BiOS) 2007* (International Society for Optics and Photonics) 64440G
[56] Sasin M E *et al* 2010 Tamm plasmon polaritons: first experimental observation *Superlattices Microstruct.* **47** 44–9
[57] Auguie B *et al* 2014 Tamm plasmon resonance in mesoporous multilayers: toward a sensing application *ACS Photonics* **1** 775–80
[58] Azzini S *et al* 2016 Generation and spatial control of hybrid tamm plasmon/surface plasmon modes *ACS Photonics* **3** 1776–81
[59] Das R, Srivastava T and Jha R 2014 Tamm-plasmon and surface-plasmon hybrid-mode based refractometry in photonic bandgap structures *Opt. Lett.* **39** 896–9
[60] Amirzada M R *et al* 2016 Surface roughness analysis of SiO_2 for PECVD, PVD and IBD on different substrates *Appl. Nanosci.* **6** 215–22
[61] Huang H *et al* 2006 Effect of deposition conditions on mechanical properties of low-temperature PECVD silicon nitride films *Mater. Sci. Eng.* A **435** 453–9
[62] Rakocevic Z, Petrovic R and Strbac S 2008 Surface roughness of ultra-thin silver films sputter deposited on a glass *J. Microsc.* **232** 595–600
[63] 2017 https://olympus lifescience.com/en/microscopes/inverted/ix83/celltirf4/
[64] Passmore D R *et al* 2014 Imaging plasma membrane deformations with ptirfm *J. Vis. Exp.* **86** 51334
[65] Schneckenburger H 2005 Total internal reflection fluorescence microscopy: technical innovations and novel applications *Curr. Opin. Biotechnol.* **16** 13–8
[66] 2017 http://olympusmicro.com/primer/anatomy/numaperture.html
[67] 2017 http://pi-usa.us/products/Microscopy_Imaging/Precision_Microscope_Stage.php
[68] 2017 https://microscopyu.com/applications/live-cell-imaging/the-automatic-microscope
[69] Hellen E H and Axelrod D 1987 Fluorescence emission at dielectric and metal-film interfaces *J. Opt. Soc. Am.* B **4** 337–50
[70] Novotny L and Hecht B 2012 *Principles of Nano-optics* (Cambridge: Cambridge University Press)
[71] Badley R, Martin W and Schneider H 1973 Dynamic behavior of fluorescent probes in lipid bilayer model membranes *Biochemistry* **12** 268–75
[72] Axelrod D, Hellen E H and Fulbright R M 2002 Total internal reflection fluorescence *Topics in Fluorescence Spectroscopy* (Berlin: Springer) pp 289–343
[73] Axelrod D 2001 Total internal reflection fluorescence microscopy in cell biology *Traffic* **2** 764–74
[74] Axelrod D 1989 Total internal reflection fluorescence microscopy *Methods Cell Biol.* **30** 245–70
[75] Wang Z *et al* 2004 Image quality assessment: from error visibility to structural similarity *IEEE Trans. Image Process.* **13** 600–12
[76] Dosselmann R and Yang X D 2011 A comprehensive assessment of the structural similarity index *Signal, Image Video Process.* **5** 81–91
[77] Liu P *et al* 2016 Cell refractive index for cell biology and disease diagnosis: past, present and future *Lab Chip* **16** 634–44
[78] McPeak K M *et al* 2015 Plasmonic films can easily be better: rules and recipes *ACS Photonics* **2** 326–33
[79] Malitson I 1965 Interspecimen comparison of the refractive index of fused silica *J. Opt. Soc. Am.* **55** 1205–9
[80] Philipp H R 1973 Optical properties of silicon nitride *J. Electrochem. Soc.* **120** 295–300